Separation and Purification Technology 356 (2025) 129825

Contents lists available at ScienceDirect

Separation and Purification Technology

journal homepage: www.elsevier.com/locate/seppur

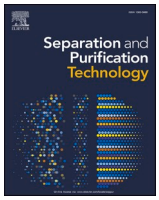

Enhancing CO_2/CH_4 separation performance in PIM-1 based MXene nanosheets mixed matrix membranes

Mohamed Yahia [a,b,c,*], Dalia Refaat [a,b], Joaquín Coronas [a,b], Carlos Tellez [a,b,*]

[a] Instituto de Nanociencia y Materiales de Aragón (INMA), CSIC-Universidad de Zaragoza, Zaragoza 50018, Spain
[b] Chemical and Environmental Engineering Department, Universidad de Zaragoza, Zaragoza 50018, Spain
[c] Chemistry Department, Faculty of Science, Helwan University, Cairo 11795, Egypt

ARTICLE INFO

Editor: Dr. S Yi

Keywords:
Intrinsic microporous polymer (PIM-1)
MXene nanosheet
Mixed matrix membrane
Gas separation
CO_2/CH_4 separation

ABSTRACT

This study presents an approach by integrating MXene nanosheets ($Ti_2C_3T_x$) into polymer of intrinsic microporosity (PIM-1) matrix to develop mixed matrix membranes (MMMs) for biogas upgrading. Different concentrations (1–5 wt%) of MXene were incorporated into PIM-1, and the resulting materials were characterized to ^1H NMR, FTIR, XRD, TGA, nitrogen adsorption, SEM and EDS to assess their physicochemical properties. The research focused on evaluating the gas separation performance, particularly CO_2/CH_4 separation, as well as the aging behavior of the MMMs. The incorporating of MXene nanosheets significantly enhanced the CO_2 permeability and selectivity of PIM-1 by enhancing gas solubility and diffusivity. The most promising results were observed at 5 wt% filler loading, achieving a 13.5 CO_2/CH_4 separation selectivity at 7652 Barrer of CO_2 permeability. In all membranes with aging time (60 days), there was a decrease in CO_2 permeability and a slight increase in CO_2/CH_4 selectivity, observing that the introduction of MXene slightly mitigates the physical aging process in the PIM-1 polymer. Additionally, the permeability tests revealed higher CO_2 permeability and (CO_2/CH_4) selectivity values for mixed gases compared to single gases. Overall, the study highlights the potential of MXene/PIM-1 MMMs as effective materials for CO_2/CH_4 separation, outperforming pristine PIM-1.

1. Introduction

Carbon dioxide (CO_2) is a prevalent component in natural gas, biogas, and is generated through the combustion of fossil fuels or coal conversion [1]. In applications involving methane (CH_4) gas the removal of CO_2 is vital to improve quality and performance, particularly in biogas production [1,2]. This step is critical for preserving energy value and preventing corrosion and adverse effects on gas compression and transportation [1,2]. Consequently, there is a pressing demand for efficient and economically viable CO_2 separation methods for CO_2 upgrading of natural gas and specially biogas, which has been shown in recent years as an alternative to fossil fuels and therefore reducing the greenhouse effect [1,2].

Various traditional industrial methods, including adsorption, absorption, membrane and cryogenic separation, have been utilized for CO_2 separation and capture [3–6]. Of these, membrane-based separation stands out due to its practicality and numerous advantages, including high productivity, easy scalability and processability, low energy demand and minimal space requirement, rendering it a desirable choice for CO_2 separation [1,2]. Consequently in CO_2/CH_4 separation, there are significant demands for membrane materials possessing high selectivity to dismiss (CH_4) losses or avoid sequential membrane stages, and high permeability to decrease membrane cost and space requirements [7–9].

Mixed matrix membranes (MMMs) combine the advantageous properties of easily processable polymeric organic materials with the excellent transport performance of specific fillers [10,11]. The objective is to develop membranes that exhibit exceptional gas permeability and highly selectivity, exceeding the so-called Robeson upper-bound line [4,5,12]. Integrating inorganic nano-fillers within a polymer framework can adjust permeability via changing solubility, molecular sieving, establishing a barrier effect, or disrupting polymer chain organization [13,14]. However, ensuring effective dispersion of nano-fillers within the polymer poses a challenge in MMM fabrication. High filler concentrations can reduce mechanical stability and specifically membrane separation performance [15,16] due to decrease in separation selectivity in poorly integrated filler-polymer MMMs, forming networks at the nano-filler-polymer interface that allow the transport of gas through less selective Knudsen-diffusion [17,18].

* Corresponding authors at: Instituto de Nanociencia y Materiales de Aragón (INMA), CSIC-Universidad de Zaragoza, Zaragoza 50018, Spain.
E-mail addresses: mohamed.yahia@science.helwan.edu.eg (M. Yahia), ctellez@unizar.es (C. Tellez).

https://doi.org/10.1016/j.seppur.2024.129825
Received 7 June 2024; Received in revised form 19 September 2024; Accepted 19 September 2024
Available online 21 September 2024

The carefully selection of both polymer and filler components is crucial, influencing the morphology and overall effectiveness of MMMs in gas separation [11,15,19], as the cutting-edge membranes with outstanding gas separation performing can be produced [15]. In this sense, intrinsic microporosity polymers (PIMs) have garnered a significant interest for their favorable gas transfer properties, specifically high permeability with acceptable selectivity. The interconnected microcavities within PIMs structures contribute to a substantial free fractional volume (FFV) and the polymer rigidity architectures [20–22]. PIM-1, the most extensively researched PIM, is notable for its ease of solubility, excellent physicochemical and thermally stable, and outstanding characteristic in the CO_2/CH_4 separation, achieving a selectivity in the approximate 12–18 range. However, PIM-1 has the disadvantage that since it is a glassy polymer in a non-stationary state, it suffers physical aging that can be mitigated by adding a filler to obtain mixed matrix membranes [23–26]. The Physical aging in PIM-1 membranes significantly affects the gas transport properties over time, particularly in terms of CO_2 permeability and selectivity. As PIM-1 ages, its polymer chains undergo structural relaxation and densification, leading to a collapse of the free fractional volume (FFV). This densification reduces the size and number of micro-voids within the polymer matrix, which are crucial for selective gas diffusion [23–26]. Consequently, the permeability of CO_2 decreases as the pathways for gas molecules become more restricted. The impact on selectivity is more complex; while the permeability of CO_2 reduces, the selectivity for CO_2 relative to other gases, such as N_2, O_2, and CH_4, can either increase or remain stable. This is due to the differential effects on diffusivity and solubility of various gases in the aged polymer. Thus, understanding the physical aging process in PIM-1 is essential for optimizing its application in gas separation technologies, as it directly influences long-term separation performance and selectivity[23–26].

Regarding the filler, various materials, including MOFs, two-dimensional (2D) nanosheets, zeolites, and silica, have been utilized as additives to improve the gas separation performing of the polymeric membranes [19,27–29]. Notably, 2D nanosheets, known for their high aspect ratio, atomic thickness, and microporous transport channels, have become a focal point in membrane separation research [30–32]. Introducing high aspect ratio nanosheets into the polymer matrix can improve contact between the polymer and filler and establish channels that facilitate high and selective molecule transport [33]. Additionally, 2D nanosheets with distinct adsorption capabilities can enhance the membrane's ability to selectively adsorb gases [34].

In recent times, a new category of 2D material, MXene, has become notable for its versatile physicochemical properties, finding extensive applications in water purification, gas separation, energy storage devices, shielding against electromagnetic interference, and various other uses [35–37]. MXene, categorized as a transition metal carbide or carbonitride, is denoted by the formula $M_{(n+1)}X_nT_x$ (where n = 1, 2, 3) [38]. Typically, MXene is obtained by selectively etching the A element from precursor MAX (formula $M_{n+1}AX_n$) powders using an acidic etching agent. Here, M stands for an early transition metal (e.g. Ti, V, Mo, Nb), X represents carbon and/or nitrogen, T_x denotes surface groups like −O, –OH, −F, and A. In the context of MAX phase materials ($M_{n+1}AXn$), where "A" is an element from groups IIIA (group 13) or IVA (group 14) of the periodic table, understanding these groups is essential [39–41]. Group IIIA includes elements like aluminum (Al) and gallium (Ga) that typically form trivalent cations, while Group IVA includes elements like silicon (Si) and tin (Sn) that form tetravalent cations. These elements impart unique properties to MAX phases, such as high thermal stability, electrical conductivity, and mechanical strength, making them crucial for advanced applications. Understanding their chemical behavior allows for tailoring MAX phases to achieve specific performance characteristics [39–41]. Various procedures have been developed for the etching of MAX, one of the most used and successful when A is Al or Si is the acid attack specifically with HF although there are trends to replace this acid with a more benign one such as HCl [42]. Due to its stable structure and micrometer lateral size, $Ti_3C_2T_x$ stands out as the most extensively studied MXene for membrane separation [43–45]. The variations in the properties of MXene nanosheets can significantly impact the characteristics of permeation of the corresponding MMMs [34,46,47]. Additionally, the choice of intercalating agent plays a crucial role in determining the effectiveness of the exfoliation process and the quality of the resulting MXene nanosheets [34,46–48].

A significant development in MXene membranes for gas separation was pioneered by Wang et al. [35], who engineered a freestanding MXene laminar membrane with well-organized nanochannels for H_2/CO_2 separation. Shen et al. [33] demonstrated the construction of ultrathin MXene laminates designed for the selective permeation of H_2 or CO_2. Liu et al. [49] presented a MXene-based membrane resilient to high temperatures, displaying favorable H_2/N_2 selectivity even at 320 °C. Various reports demonstrated MXene nanosheets as a filler for membrane gas separation [34,46,47,50–53], but specifically the utilization of MXene as filler in constructing MMMs based on polymer PIM-1 for gas separation has been explored only for CO_2/N_2 separation [54].

Herein, this study introduces a novel approach for CO_2/CH_4 separation by the synthesis of MXene nanosheets by a procedure based on the use of HCl, more benign than common HF, and its incorporating into a PIM-1 network with various loadings (1–5 wt%). The generated MXene/PIM-1 MMMs were assessed for their CO_2/CH_4 separation efficiency and aging. In addition, to unravel the physical–chemical processes studied, the membranes and materials were characterized by various techniques that include ^{1}H NMR, FTIR, TGA, XRD, nitrogen adsorption and SEM-EDS. The present research emphasizes the capability of MMMs comprising MXene nanosheets and PIM-1 as remarkably effective materials for CO_2/CH_4 separation surpassing pristine PIM-1.

2. Experimental

2.1. Materials

MXene sheets were synthesized by using titanium aluminum carbide/Ti_3AlC_2, lithium chloride/LiCl, and hydrochloric acid/HCl, all chemicals supplied from Sigma-Aldrich with high purity (99 %). PIM-1 was prepared using top-quality chemicals, each with a purity ≥ 99 %. These chemicals, such as methanol-MeOH, potassium carbonate anhydrous/K_2CO_3, N-methyl-pyrrolidone/NMP, toluene/Ph-CH_3, and chloroform-$CHCl_3$ were acquired from Sigma-Aldrich. Additionally, tetrafluoro-terephthalonitrile/TFTPN and tetra-methyl-1,1′-spirobiindane-5,5′,6,6′-tetraol/TTSBI were supplied from the same source, before PIM-1 synthesizing, TFTPN was recrystallized in (MeOH) and TTSBI was sublimated at 150 °C.

2.2. Procedures

2.2.1. Syntheses of PIM-1 and MXene nanosheets

PIM-1 was produced using a previously established protocol [14,19,55], refer to the supplementary information, the produced PIM-1 was utilized in a previous study and its detailed characterization can be referenced there [19]. In the synthesis, TFTPN and TTSBI (0.01 mol each) were mixed with anhydrous K_2CO_3 (0.03 mol), NMP (20 mL), and Ph-CH_3 solvent (10 mL) in a nitrogen-purged three-neck flask under continuous stirring and refluxing at 160 °C for 4–5 h, resulting in a thick solution that was then precipitated in MeOH. The polymer was dried, dissolved in $CHCl_3$, and re-precipitated multiple times in MeOH. To ensure thorough purification, the polymer was soaked in MeOH overnight before being dried in a vacuum oven at 80 °C overnight.

To synthesize MXene nanosheets, a MXene ($Ti_3C_2T_x$) powder was initially produced following a previously established methodology [56,57] with little modification. Briefly, LiCl (1 g) was dissolved in HCl solution (20 mL, 6 M) in a glass beaker (250 mL) inside an ice bath. Following this, 1 g of MAX powder (Ti_3AlC_2) was gradually introduced into the beaker under a constant stirring at 35 °C for 24 h. The resulting

product was washed with deionized water and centrifuged multiple cycles (5-cycles) at 5,000 rpm, resulting in a visible sediment, then the sediment was subjected to repeated cycles of dispersion in 50 mL of DI water, sonication, and centrifugation until the supernatant pH value reached ≈ 7 to yield delaminated MXene (nanosheets). In the end, the exfoliated MXene nanosheets were separated from unexfoliated ones, which remained in the supernatant, by vacuum filtration with continuous washing with deionized water, then the obtained exfoliating MXene nanosheets were subjected to drying under vacuum oven (overnight, 80 °C).

2.2.2. Fabrication of MMMs

Initially, PIM-1 (0.1 g) was dissolved in $CHCl_3$ (5 mL). Subsequently, MXene nanosheets were dispersed in $CHCl_3$ by sonication utilizing an ultrasonic bath for 1 h. To constitute 1–7.5 wt% MXene MMMs, the mixtures of PIM-1 solution and MXene dispersed solution were agitated for an additional 3 h. Subsequently, the suspensions generated were poured into glass Petri dishes and left under the fuming hoods for 3 days to allow the solvent to evaporate completely at room temperature. Prior to membrane testing, involving both pure PIM-1 and MMMs, the dried membranes underwent a 30 min immersion in MeOH, followed by overnight drying in a vacuum oven at 60 °C. The membranes were then stored in a dark, room-temperature environment. MXene/PIM-1 (1–5 wt %) MMMs were evaluated for gas separation performance, whereas the MXene/PIM-1 (7.5 wt%) MMM was fabricated and excluded from testing due to its compromised mechanical properties and aggregation tendencies.

2.2.3. Characterization of PIM-1 powder and MXene/PIM-1 MMMs

The ^1H NMR analysis was conducted using a Bruker Avance III 400 spectrometer at a proton frequency of 400 MHz and 25 °C, with $CDCl_3$ serving as the internal reference. For molecular weight analysis of PIM-1, gel permeation chromatography/GPC was performed coupled with multi-angle light scattering/MALS detection. Fourier transform infrared spectroscopy/FTIR analysis was applied using a Bruker Vertex 70 FTIR spectrometer connected with a DTGS detector and a ATR diamond accessory with a wavenumber resolution of 4 cm^{-1} measured in the range 4000–600 cm^{-1}. Thermogravimetric analyses/TGA was undertaken with a Mettler Toledo TGA-STDA 851e instrument under N_2 atmosphere. To assess crystallinity, X-ray diffraction/XRD was executed using a Panalytical Empyrean apparatus with CuK_α radiation ($\lambda = 0.154$ nm), scanning between (5-40°) at a scan rate (0.03° s^{-1}). Nitrogen isotherms at −196 °C were recorded using a Micromeritics Tristar 3000, and the specific surface area (SSA) of the porous materials (PIM-1 and MXene nanosheets) was determined via the Brunauer-Emmett-Teller/BET method. Scanning electron microscope-SEM images of the membranes were captured applying an Inspect F50 model-FEI operating at 10 kV. The membrane thickness, measured at five different positions with a micrometer scale, was in the approximate 65–100 μm range.

2.2.4. Gas permeation measurements

For CO_2/CH_4 separation, a circular membrane with an area (2.12 cm^2) was located in a module with dual stainless-steel pieces and a macro-porous disc support (model 316LSS, 20 μm pore size). The membranes were clamped and sealed within the permeation module using Viton o-rings, and the temperature was maintained at 35 °C by putting the module in an oven (Memmert). The gas separation tests were conducted with a CO_2/CH_4 mixture (50/50 ratio), delivered at 3 bar pressure to the feed side. Two Alicat Scientific mass-flow controllers (MC-100CCM-D) managed the flow rates, set to 50 $cm^3(STP)\cdot min^{-1}$ for each gas. On the permeate side, helium (He) was used as a sweep gas at a rate of 2 $cm^3(STP)\cdot min^{-1}$, maintained at atmospheric pressure (~1 bar) by another mass-flow controller (MC-5CCM-D). The concentrations of CO_2 and CH_4 in the permeate were continuously analyzed using a TCD in a micro-gas chromatograph (Agilent 3000A). Additional information regarding the utilized equipment was provided in our previous work [19,58] and schematically was represented in Fig. 1. The permeabilities of gases were quantified in Barrer units (10^{-10} $cm^3(STP)\cdot cm\cdot cm^{-2}\cdot s^{-1}\cdot cm\cdot Hg^{-1}$). This involved flux (flowrate divided by the area of the membrane), partial pressure, and multiplying by the membrane thickness (Eq.1). The selectivities were calculated as the ratio of the corresponding permeabilities (Eq.2).

$$P_{gas} = \frac{Flux_{gas}(cm^3(STP)\cdot cm^{-2}\cdot s^{-1})\cdot Thickness(cm)}{\Delta P_{gas}(cmHg)} \quad (1)$$

$$\alpha = \frac{P_{CO2}}{P_{CH4}} \quad (2)$$

To assess how aging affects the membrane separation performance, the membranes were stored in a dry container for 60 days to prevent exposure to moisture. Afterward, the gas permeation experiments were conducted on the aged membranes without treating them with MeOH. Each membrane underwent five repeated measurements both before and after the aging period for ensuring precise results and know the corresponding errors.

Furthermore, the time-lag experiments were conducted for a duration to ensure accurate measurements (3-times at least). To satisfy the boundary conditions of the time lag method and achieve a steady-state flux, the downstream pressure was maintained at a much lower level than the upstream pressure, with a maximum downstream pressure set at 0.1 % of the upstream pressure. The experiment was concluded once this threshold was reached. Permeability (P) was calculated from the slope of the pressure–time (p_d/t) curve in the steady-state region. The diffusion coefficient (D) was determined using the time lag method, and the solubility coefficient (S) was derived from the calculated P and D values [59–61]. More details about the time lag method measurements and calculations are provided in our previous work [61]. The time lag experimental setup (Fig. S1) and the equations performed for calculating D, P, and S are represented in the supplementary information.

3. Results and discussion

The structural verification of PIM-1 was accomplished through the examination of its ^1H NMR and GPC spectra as illustrated in our previous work [19]. FTIR spectroscopy was performed on both PIM-1 and PIM-1/MMMs (Fig. 2) to explore the interactions between MXene nanosheets and PIM-1. For PIM-1, the obtained FTIR spectrum agreed with the previous published studies [11,14,55]. The absorption bands at 2240 cm^{-1} and 1260 cm^{-1} in the PIM-1 membrane spectrum are linked to nitrile groups, specifically the C≡N stretching and (C-N) bending modes, respectively [14,55]. Moreover, the absorptions in the range of 2850–2950 cm^{-1} and 1445 cm^{-1} are associated with methylene (CH_2) stretching and (C=C) aromatic stretching vibration modes, respectively [14,55]. The C-N stretching mode corresponds to the 1350–1250 cm^{-1} region. The peak identified at 1009 cm^{-1} is a result of the characteristic C–O aliphatic stretching mode, whereas that at 870 cm^{-1} is linked to the aromatic sp^2 C–H bending.

In MXene nanosheets spectrum, three obvious peaks at 3500–3200, 1650, and 835–621 cm^{-1} are linked to (–OH), (C-O), and (Ti-O) stretching vibration, respectively, indicating the terminal (–OH) groups on the MXene surface [62,63]. In the PIM-1/MXene MMMs (2.5–7.5 wt %) spectra, both the characteristic peaks of PIM-1 and those of MXene can be observed. It is referred that the (–OH) peak of PIM-1/MXene MMMs mainly comes from MXene nanosheets, which indicates that hydrogen bonds might be formed between the PIM-1 polymer chains and the high polarity MXene nanosheets surface [64].

Additionally, the FTIR analysis revealed no noteworthy variations or shifts in the distinctive bands for PIM-1 and MXene with varying loadings (2.5 and 5 wt%) of MXene in the MMMs. This observation suggests that both materials were uniformly dispersed and chemically stable within the prepared membranes without significant changes in their

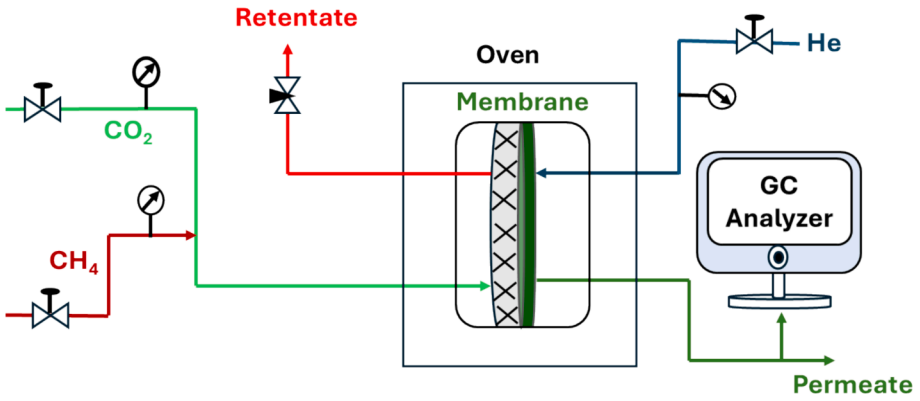

Fig. 1. The schematic diagram represented the experimental set-up used for the CO_2/CH_4 mixture separation.

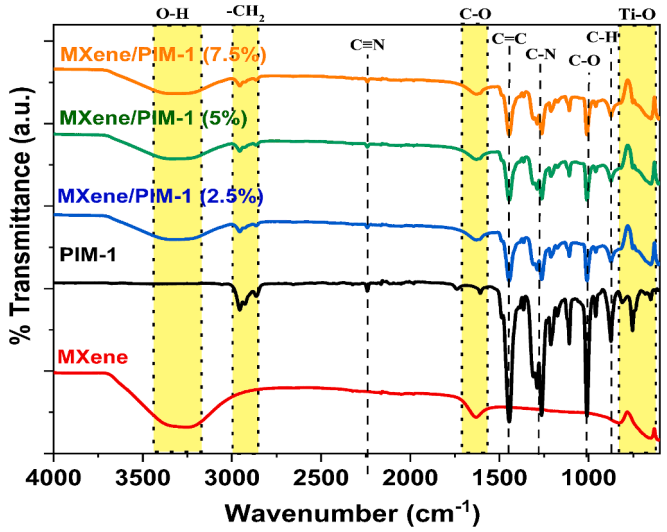

Fig. 2. FTIR spectra for PIM-1, MXene nanosheets and PIM-1/MXene MMMs (2.5, 5, and 7.5 wt%).

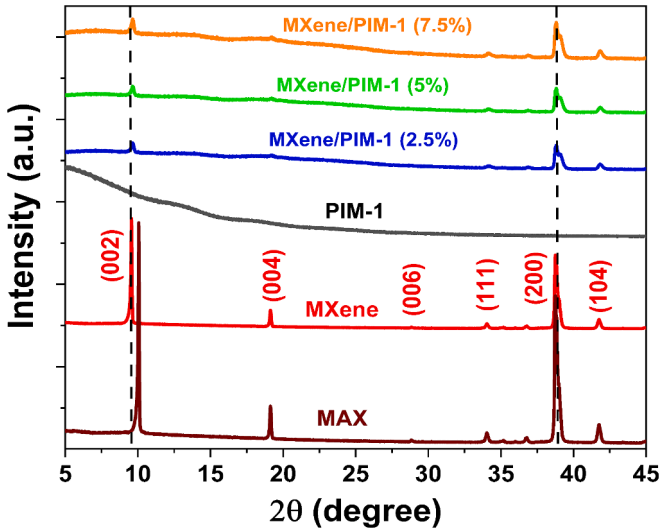

Fig. 3. XRD patterns of PIM-1 (powder), MXene nanosheets and MXene/PIM-1 MMMs (2.5, 5, and 7.5 wt%).

absorption bands. These results suggest that the two materials can be incorporated within the MMMs without altering their chemical structures. Furthermore, the FTIR analysis for MXene/PIM-1 (7.5 wt%) confirmed that there were no significant changes in the absorption bands compared to lower loadings (2.5 % and 5 %), as shown in Fig. 2. However, the higher loading of 7.5 % led to degradation and reduced mechanical properties in the MXene/PIM-1 (7.5 wt%) MMM, as illustrated in Fig. S3, likely due to the agglomeration of MXene particles at higher concentrations, disrupting the polymer matrix.

Although the IR analysis shows no noticeable shifts in the main peaks, likely due to the low filler loadings, other types of interactions may still be present. These "favorable interactions" include hydrogen bonding, van der Waals forces, and π-π interactions, rather than stronger covalent or coordination bonds, and they contribute to the improved properties of the MXene/PIM-1 MMMs.

Fig. 3 shows the XRD diffractogram of PIM-1 displaying its amorphous structure. The two broad peaks at ca. 13.4° and 18.0° correspond to chain-to-chain distances of 0.49 nm and 0.65 nm, respectively, associated with the efficient chain packing featuring a microporous architecture within PIM-1 matrix [14,55,65]. Also, Fig. 3 shows the typical XRD diffractogram of MXene nanosheets with peaks at 2θ values of approximately 9.5°, 19.5°, 28.5°, 35.9°, 39.8° and 43.6°, which linked to the crystalline planes (002), (004), (006), (111), (200) and (104), respectively [34,46,47]. Applying Bragg's law to the peak of the (002) plane results in a d-spacing of 0.93 nm. However, the initial MAX powder showed similar crystal patterns, including a notable appearance of the crystalline plane (002) at 2θ ≈ 9.9°, i.e. showing an evident displacement to lower angles-larger d-spacings meaning from 0.89 nm in MAX to 0.93 nm in MXene. This indicates some intercalation of polar lithium-based species but the small decrease of peak intensities respect MAX suggests an important prevalence of the initial crystalline layered structure meaning minimal exfoliation of MXene nanosheets during the etching of MAX powder with LiCl. Additionally, the XRD patterns of MXene/PIM-1 MMMs in Fig. 3, revealing subtle indications of PIM-1 features, are consistent with the MMMs maintaining the same chain-to-chain distances of 0.49 nm and 0.65 nm as in the original polymer, indicating minimal alterations to the polymeric structure following the inclusion of MXene crystals. However, noticeable peaks of the MXene crystals at approximately 9.7° and 39.8° 2θ values, corresponding to the crystalline planes (002) and (200), respectively, are evident in the diffractograms. Also, the XRD analysis showed no significant changes or shifts in the characteristic diffraction patterns of PIM-1 and MXene across different loadings, up to 7.5 wt% of MXene in the MXene/PIM-1 MMMs. This is consistent with a successful integration of MXene nanosheets within the MMMs without any noticeable loss of their crystallinity.

Gas-sorption analysis was applied to evaluate the micro-porosity of both evacuated PIM-1 and MXene nanosheets. In agreement with a combination type I and IV isotherm shown in Fig. 4, PIM-1 exhibits a notably high BET specific surface area (SSA, 750 $m^2 \cdot g^{-1}$), providing a

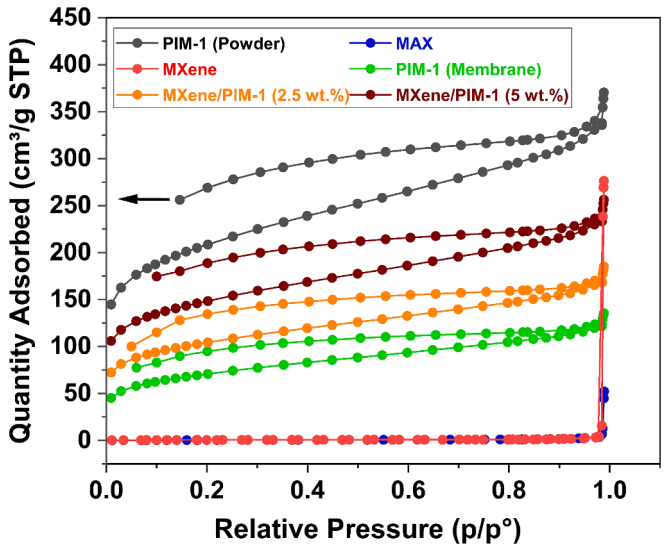

Fig. 4. N_2 isotherms at −196 °C for PIM-1, MXene nanosheets, MAX particles, PIM-1 membrane and MXene/PIM-1 (2.5 and 5 wt%) MMMs.

robust evidence of its microporous characteristics and its capacity for adsorption and desorption of N_2 gas, consistent with previous literature [66–68]. At medium P/P_0, the hysteresis observed indicates the presence of mesopores within PIM-1 [14,69]. The hysteresis that continues at low pressure is usually found in microporous polymers and has been related, according to studies, to swelling or diffusional limitations due to the blocking of pores, also indicating a pronounced hysteresis and greater connectivity between the pores, which is undoubtedly of interest for membrane separation processes [70]. Also, the data in Fig. 4 allowed the calculation of the BET SSA for MXene nanosheets (16.3 $m^2 \cdot g^{-1}$) and MAX particles (2.2 $m^2 \cdot g^{-1}$), which display a notably lower value than typical for 2D materials [37,46,47], aligned with previous reports [71,72]. The lower BET SSA for MXene and MAX comparted within other 2D materials can be attributed to the surface of MXene being commonly terminated with functional groups such as hydroxyl (–OH), chloride (−Cl), or oxygen-containing groups and the density and type of these functional groups can influence the overall surface chemistry and, consequently, the surface area available for specific interactions [37,46,47,71]. The increase in the surface area of MXene with respect to MAX indicates a certain degree of exfoliation. Furthermore, the pronounced increase in adsorption of MXene versus MAX at P/P_0 close to 1 indicates an increase in capillary condensation between particles which may be related to indicated exfoliation. In any event, even if the exfoliation of the parent material was limited, the increase of the BET SSA together with the mentioned XRD supported intercalation allow to predict an improved filler-polymer interaction helping the enhancement of the gas separation performance shown below.

Furthermore, the gas-sorption analysis was applied to evaluate the specific surface area (SSA) of both evacuated PIM-1 membrane and MXene/PIM-1 MMMs as represented in Fig. 4 and Table S1 (supplementary information). The BET SSA values reveal a significant variation between PIM-1 in its powder form, membrane form, and when combined with MXene nanosheets as MXene/PIM-1 MMMs. The PIM-1 powder exhibits a notably high BET specific surface area (750 $m^2 \cdot g^{-1}$), indicative of its microporous nature as mentioned before [66–68]. However, when PIM-1 is processed into a membrane, the BET SSA decreases substantially (351 $m^2 \cdot g^{-1}$). This reduction can be attributed to the densification and partial collapse of the microporous structure during the membrane formation process, which leads to tighter packing of polymer chains and a reduction in the accessible surface area [73,74]. In contrast, the incorporation of MXene nanosheets into the PIM-1 matrix results in an increase in the BET SSA of the MXene/PIM-1 MMMs. Specifically, the BET SSA increases to 410 $m^2 \cdot g^{-1}$ for the MXene/PIM-1 (2.5 wt%) and further to 451 $m^2 \cdot g^{-1}$ for the MXene/PIM-1 (5 wt%). This increase is likely due to the exfoliation of MXene nanosheets within the PIM-1 matrix, which enhances the accessible surface area. Additionally, the inclusion of MXene nanosheets may disrupt the polymer structure, creating additional micro- and mesopores that contribute to the increased surface area [50–54], reverting in part the above mentioned collapse. The observed enhancement in BET SSA with increasing MXene content underscores the role of MXene nanosheets in improving the porosity and potentially enhancing the gas separation performance for the fabricated MXene/PIM-1 MMMs [50–54].

Fig. 5 displays the TGA curves for PIM-1, MXene and MXene/PIM-1 MMMs. The presence of nitrile-containing groups (C-N) within the PIM-1 structure leads to enhanced thermal stability for PIM-1 up to 400–450 °C, which is attributed to the robust dipolar interactions with the nitrile functional groups [14,55]. Then, the decomposition process for PIM-1 was observed above 450 °C is attributed to the degradation of the polymer components [14,55]. Moreover, as illustrated in Fig. 5, MXene displays two distinct stages of weight loss. The initial stage, occurring between 100–200 °C, primarily results from the evaporation of water absorbed in MXene, originating from its numerous surface hydroxyl functional groups. Subsequently, the mass loss observed between 200–800 °C is attributed to the breakdown of MXene functional groups. The entirety of weight loss witnessed in MXene, approximately ranging between 10 % and 15 % throughout the whole heating process, underscores its remarkable thermal robustness [57]. It can be seen how the MAX material has hardly any weight loss, so the indicated losses would indicate the presence of functional groups and evidence of the variation from Ti_3AlC_2 towards MXene. The thermal stability of PIM-1/MMMs closely resembles that of the PIM-1 membrane, suggesting the absence of a filler catalytic effect on the polymer degradation, as observed in other examples, of course with a much higher filler content [75]. The observed reduction in weight of approximately 5–10 % in the MMMs at temperatures between 100 and 300 °C is attributed to the release of solvent and gas molecules trapped within the MMM structures, these molecules primarily retained within the MXene functional groups [11,19,76,77] and in the MXene-PIM-1 interfaces. The subsequent decrease in weight observed around 475–700 °C is attributed to the decomposition of residues within the PIM-1/MMMs [14,55]. In addition, the TGA analysis showed no significant changes in the thermal stability of MXene/PIM-1 MMMs with different loading of MXene nanosheets in the MMMs. This suggests a successful incorporation of

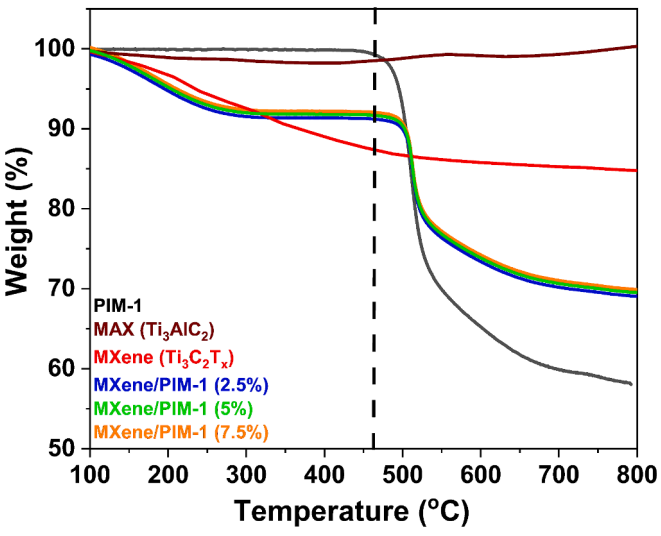

Fig. 5. TGA curves for PIM-1, MXene and MXene/PIM-1 MMMs (2.5, 5, and 7.5 wt%).

MXene nanosheets into the MMMs without any noticeable impact on their thermal decomposition behavior.

Fig. 6 illustrates the outcomes of SEM analysis conducted on PIM-1, pristine MAX (Ti_3AlC_2) and the synthesized MXene nanosheets ($Ti_3C_2T_x$). Fig. 6a-c provide insights into the morphological surface, revealing the microporosity characteristics observed in the N_2 isotherm, of the PIM-1 matrix (Fig. 6a), which align with findings from prior investigations [14,19,65] and in agreement with the finding observed within Fig. S2a and Fig. S2b (supplementary information), which provide more additional information about the microporosity within PIM-1 membrane. In the SEM images of the pristine MAX powder (Fig. 6b) and the synthesized MXene nanosheets (Fig. 6c), it is evident that post Al-etching from the pristine MAX powder, the MXene nanosheets exhibit a layered accordion-like structure, with the layers distinctly separated, indicating successful exfoliating of MAX powder with LiCl to produce the MXene nanosheets. While the synthesized MXene nanosheets demonstrate a lamellar structure with numerous interlayer channels, there remains some agglomeration in the etched MXene nanosheets.

The SEM images corresponding to the MMM at 5 wt% (see Fig. 7a-b) indicate the favorable interactions between the MXene nanosheets and PIM-1, showing a Mxene particle agglomerate perfectly surrounded by polymer [19,43,46,50]. This suggests a MXene nanosheets-polymer interaction which could be attributed to their chemistry, characterized by a higher existence of functional groups, such as hydroxyl groups, which, helped by the high aspect ratio of the particles, likely facilitating interactions with the polymer chains. This is anticipated to offer enhanced affinity and selective channels, leading to superior CO_2/CH_4 separation performance through the MXene/PIM-1MMM [34,46,47]. Furthermore, Fig. 7 indicates a minimal exfoliation for MXene nanosheets within the MXene/PIM-1 MMMs, owing to the lower chemical reactivity nature of LiCl compared to LiF, which may result in reduced exfoliation efficiency as discussed above. This lower reactivity due to the small ionic strength for LiF as compared to LiCl, which provide more electronegative fluoride ions with stronger electrostatic interactions with MAX phase layers, enhancing intercalation and exfoliation compared to LiCl [48,78].

Furthermore, Fig. 7 displays the elemental composition of the MXene/PIM-1 MMM with 5 wt% MXene, as determined by SEM-EDS analysis. The EDS mapping images (Fig. 7 c–e) show the distribution of titanium (Ti), which is a key element of the MXene nanosheets. The Ti mapping confirms, together with the layered structure observed and the EDS analysis, the presence of MXene nanosheets.

Furthermore, the SEM images in Fig. S2 demonstrate the microporosity and MXene dispersion within the PIM-1/MXene composite membrane. Fig. S2a and S2b show the porous structure of the PIM-1 membrane at higher magnification, revealing interconnected voids that are characteristic of PIM-1′s intrinsic microporosity. These micropores arise from the rigid polymer backbone, creating sub-nanometer voids essential for gas separation. Fig. S2c provides a full cross-sectional view of the MXene/PIM-1 membrane, confirming the examination of the entire section. The EDS mapping in Fig. S2e highlights the distribution of titanium (Ti), confirming the uniform dispersion of $Ti_3C_2T_x$ MXene within the membrane. This even distribution is further supported by the EDS spectrum in Fig. S2f, indicating successful MXene incorporation. The homogeneity of MXene throughout the membrane ensures its improved mechanical and functional properties without agglomeration. Together, these SEM images with Fig. 6 confirm both the microporous structure of PIM-1 and the uniform dispersion of MXene.

Furthermore, Fig. S3 (supplementary information) illustrates the mechanical integrity of the fabricated membranes (PIM-1 and MXene/PIM-1 (5 wt%) MMMs), evaluated via a manual stretch test. This test cautiously involved stretching the membrane by hand to gauge its resilience and robustness. The outcomes of this manual evaluation demonstrate that the MMM with optimal loading MXene filler 5 wt% possesses promising mechanical properties and strength. Increasing filler loading beyond 5 wt% led to degradation and cracking within the MXene/PIM-1 (7.5 wt%) composite as shown in Fig. S3.

3.1. The mixed gases separation performance

Table S2 and Fig. 8 show the CO_2 permeability and CO_2/CH_4 selectivity results for both pristine PIM-1 and MXene/PIM-1 (1–5 wt%) MMMs. CO_2 permeability and CO_2/CH_4 selectivity depict better values with MXene/PIM-1 MMMs with higher MXene nanosheets loading (5 wt %) as compared to lower loadings (1–2.5 wt%). Before aging, integrating MXene nanosheets into PIM-1 led to an enhancement in the CO_2 permeability, rising from around 6085 Barrer to a range of 6816–7652 Barrer for MXene/PIM-1 MMMs. Moreover, the CO_2/CH_4 selectivity increased from 8.7 to (11.4–13.5) for MXene/PIM-1 MMMs. This improvement can be attributed to the beneficial effect of embedding MXene nanosheets within the PIM-1 matrix, creating preferential and selective channels that facilitate the selective gas diffusion during the separation process [34,46,47,50], even at the relatively low content of filler (always below 5 wt%). These channels are related to the spaces present in the MXene agglomerates and to the MXene particle-polymer interfaces in which the good filler polymer interaction favors the creation of selective and fast CO_2 pathways (as compared to the bare polymer with lower permeability and selectivity values).

Additionally, the findings presented in Table S2 (supplementary information) and Fig. 8 highlight the divergent impacts on the CO_2 and CH_4 permeabilities by incorporating MXene nanosheets into the PIM-1 matrix membrane. With CO_2 and CH_4 kinetic diameters 0.33 nm and 0.38 nm, respectively, the former is favored for selective transport, this

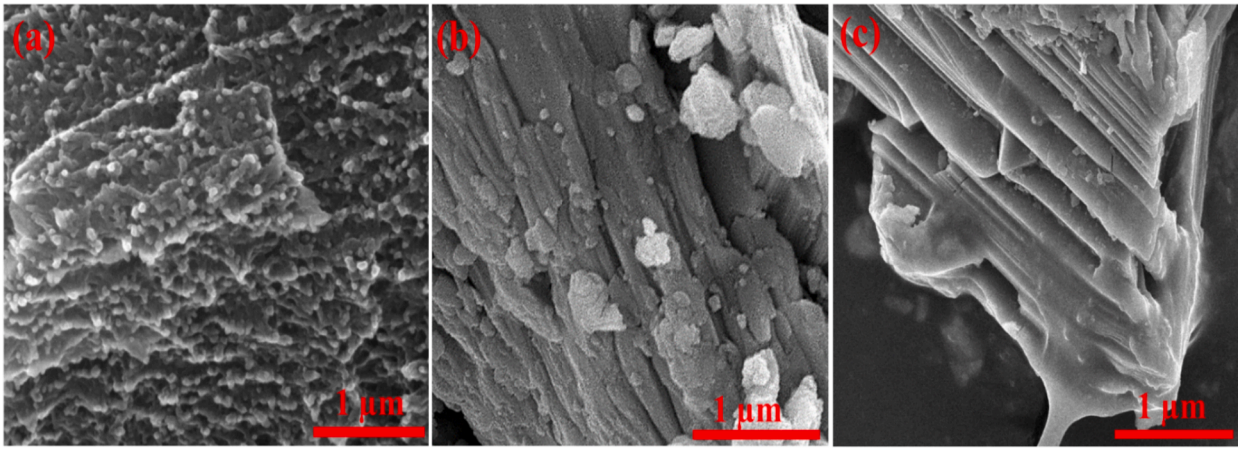

Fig. 6. SEM images for: (a) PIM-1 pristine membrane, (b) Pristine MAX powder, (c) The synthesized MXene nanosheets.

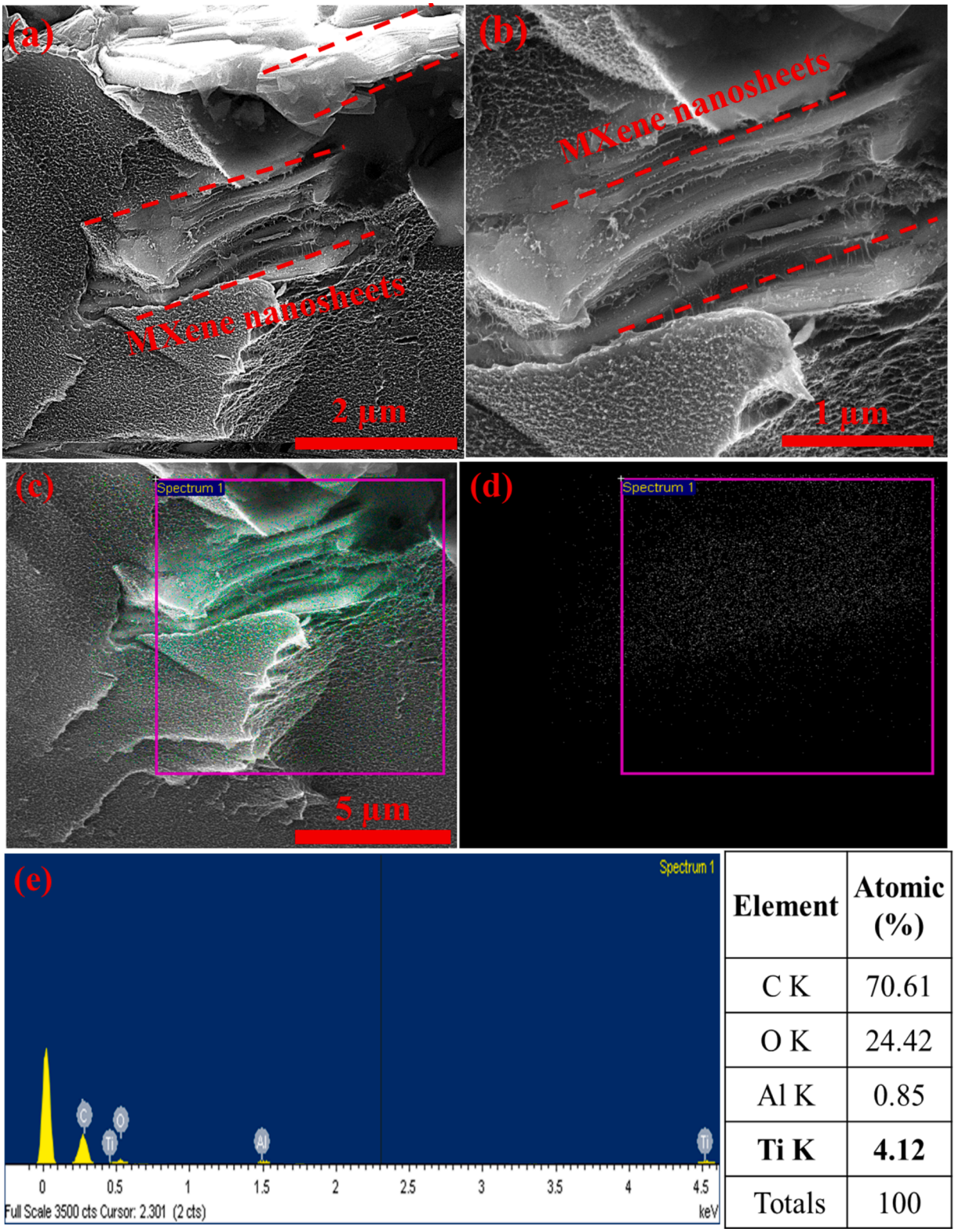

Element	Atomic (%)
C K	70.61
O K	24.42
Al K	0.85
Ti K	**4.12**
Totals	100

Fig. 7. SEM cross-section images for MXene/PIM-1 (5 wt%) (a-b), EDS-SEM images for MXene/PIM-1 (5 wt%) (c–e) evidencing the presence of Ti ($Ti_3C_2T_x$) within the membrane.

enhancement is further facilitated by the microporous structure inherent in the PIM-1 matrix [14,19,55,79]. Furthermore, the MXene nanosheets exhibit a narrow porosity of 0.32 nm [80,81], exerting a barrier effect which favors the CO_2 transport over that of CH_4, in agreement with Fig. 8. Additionally, the abundant polar groups in MXene surface influence PIM-1 ability to capture CO_2 more than CH_4, while MXene layered structure assists in the efficient diffusion of CO_2 through the membrane [46,47,50,57,82]. Certainly, it was noted that CO_2 molecules displayed a higher permeability throughout the MXene/PIM-1 MMMs in comparison to CH_4 molecules. This trend may also be assigned to the CO_2 quadrupole moment interacts electrostatically with the interaction sites of the MXene nanosheets, particularly the terminal –OH groups

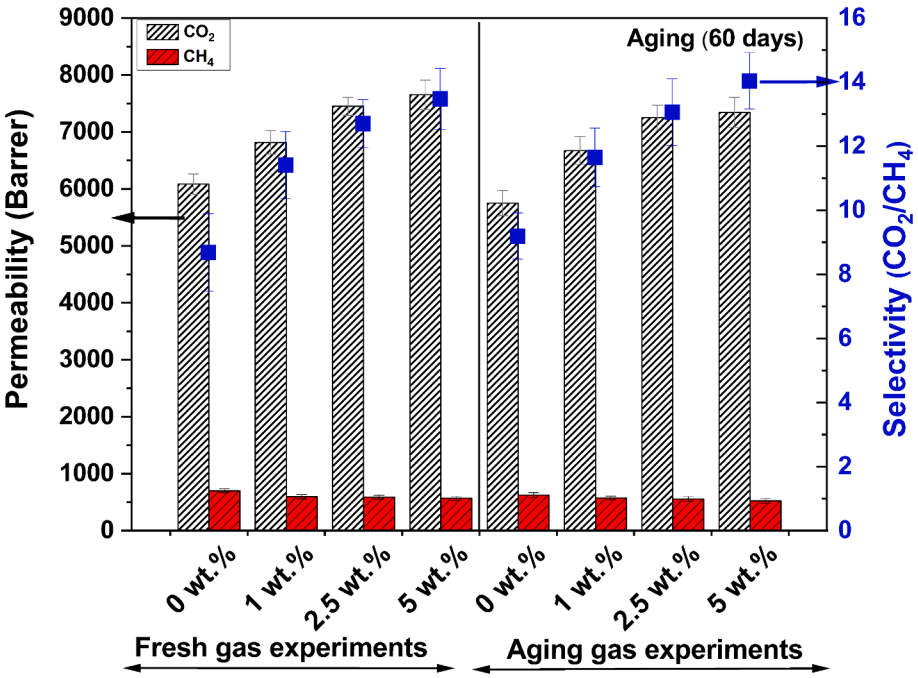

Fig. 8. CO_2 permeability and CO_2/CH_4 mixed selectivity evaluated before and after (60 days) aging for both pristine PIM-1 and MXene/PIM-1 (1–5 wt%) MMMs. Permeability and selectivity data can be found in Table S2.

present on their surface [50,57,82–84]. This is consistent with the CO_2-philicity of PIM-1 and the highly polar nature of the MXene nanosheets surface. These factors contribute to increasing CO_2 solubility in the MMMs, consequently improving the CO_2/CH_4 selectivity, as observed in prior studies on other PIM-1 MMMs [14,19,24].

The aging behavior of the membranes under investigation, including both pristine PIM-1 and MMMs, was also assessed. After a 60-day aging period (membranes stored at room temperature without exposure to light), all MMMs showed a decrease in CO_2 permeability and a slight improvement in CO_2/CH_4 selectivity (refer to Table S2 and Fig. 8). Previous studies have indicated that PIM-1, renowned for its high FFV, undergoes physical aging, resulting in a noticeable decline in permeability over time, accompanied by a minor improvement in selectivity [25,85–87]. This aging phenomenon is frequently observed in polymers of the PIM type [88], where the polymer structure regularly reorients locally towards an equilibrium pseudo-state. This local reorganization effects in a significant decrease in FFV, resulting in reduced membrane permeability and a slight improvement in selectivity [25,85–88]. After evaluating the performance of the MMMs both before and after aging, a consistent trend emerged as permeability decreased while selectivity increased, aligning with the upper-bounds (UBs) correlation [3,4]. It is worth noting that the aging process predominantly impacts the characteristics of PIM-1 [14,18], and the MXene/PIM-1 MMMs also undergo considerable aging processes, as evidenced by earlier studies on PIM-1 MMMs [89–91]. In any case, the decline in CO_2 permeability due to aging follows this trend: PIM-1 (5.5 % decrease) > MXene/PIM-1 MMMs (2.1–4.0 % decrease, notably with a significant 4 % decrease observed at the 5 wt% loading). However, this is balanced by an overall increasing in CO_2/CH_4 selectivity, with MXene/PIM-1 MMMs showing an increase of 2.0–4.3 %, the highest increase of 4.3 % obtained at the highest loading of 5 wt%, compared to an increase of 5.9 % for PIM-1. It is evident that the most favorable separation performance was achieved with the 5 wt% MXene/PIM-1 MMMs, exhibiting a CO_2 permeability of 7652 Barrer and a CO_2/CH_4 selectivity of 13.5 before the physical aging and CO_2 permeability of 7345 Barrer and a CO_2/CH_4 selectivity of 14.0 after the physical aging. This positive result after aging indicates that the interactions between the polymer and MXene filler in the MMMs help counterbalance the intrinsic flexibility of the polymer chains. MXene's unique 2D structure and surface functionalities can interact with the polymer matrix, potentially reducing chain entanglements and creating additional free volume (FFV). This can enhance the local flexibility of polymer segments, improving gas transport properties in terms of selectivity [18,87,88], because the MXene particles slightly restrict the movement of the polymer architecture. Additionally, this restriction of chain movement by MXene helps mitigate physical aging [24].

Additionally, single gas permeability tests were performed for both pristine PIM-1 and MXene/PIM-1 (1–5 wt%) MMMs, with the outcomes summarized in Table S3 (supplementary information) and depicted in Fig. S4a for permeability and Fig. S4b for CO_2/CH_4 selectivity. It is important to note that the mixed gases exhibit elevated CO_2/CH_4 selectivity and CO_2 permeability in comparison to the single gases [19,24,61,92,93]. This behavior is ascribed to the microporous characteristics of PIM-type membranes, which enables selective gas diffusion and sorption based on its polarity and molecular size. In mixed gas environments, there is a competition between gases with varying properties within the micropores. This competition enhances selectivity because the more permeable gas tends to occupy these areas preferentially, impeding the diffusion of less permeable gases [19,24,61,92,93]. Additionally, interactions between various gas molecules in mixed gases create synergistic effects, resulting in higher overall permeability and selectivity in comparison scenarios involving individual gases [19].

Furthermore, the obtained results demonstrate notable differences in the behavior of PIM-1 and MXene/PIM-1 MMMs when exposed to single and mixed gases, particularly in terms of CO_2 permeability and CO_2/CH_4 selectivity. In mixed gas environments, both CO_2 permeability and CO_2/CH_4 selectivity are higher for MXene/PIM-1 MMMs compared to neat PIM-1 before aging. This suggests that the inclusion of MXene enhances the separation performance. After aging, the decrease in permeability is less pronounced in MXene/PIM-1 MMMs, indicating that MXene helps mitigate the effects of physical aging while selectivity remains stable or slightly improved. In single gas tests, MXene/PIM-1 MMMs similarly show higher CO_2 permeability and CO_2/CH_4 selectivity compared to the neat PIM-1 before aging, with consistent improvements across the different MXene loadings. Although the reduction in CO_2 permeability is more significant in single gas tests after aging, MXene/PIM-1 MMMs still demonstrate better aging resistance compared to neat PIM-1, with stable

or slightly improved selectivity. Furthermore, the experimental errors were carefully considered to ensure the reliability of these findings, as indicated by the standard deviations in Tables S1 and S2. For mixed gases, the standard deviations of CO_2 permeability before aging range from ± 155 to ± 258 Barrer, and for CO_2/CH_4 selectivity, they range from ± 0.8 to ± 1.2. After aging, the standard deviations for CO_2 permeability are slightly higher, reflecting increased variability due to aging effects, but remain within a reasonable range.

For single gases, the standard deviations for CO_2 permeability before aging range from ± 184 to ± 231 Barrer, and for CO_2/CH_4 selectivity, they range from ± 0.9 to ± 1.2. Similar to mixed gases, the standard deviations after aging show a slight increase, particularly for CO_2 permeability. Overall, the experimental errors for both mixed and single gases are consistent and within acceptable limits, indicating reliable and reproducible measurements. The slightly higher errors observed after aging reflect the natural variability introduced by aging processes, but the data still clearly demonstrate the performance advantages of MXene/PIM-1 MMMs over neat PIM-1.

Furthermore, the CO_2 permeability and CO_2/CH_4 selectivity values for neat PIM-1 reported in this research work are consistent with the reported values for PIM-1 in the literature [14,79,93–97], which indicate a CO_2 permeability in the range of 5000–9000 Barrer and a selectivity in the range of 6.5–16, which fall within the expected range. The observed lower transport properties can be attributed to the inherent physical aging of PIM-1, which leads to a decrease in free volume over time and thus reduced permeability. Additionally, variations in process history, such as differences in casting solvent, thermal treatment, and storage conditions, mixture separation pressure, and gas mixture ratio can influence as well the gas transport performance. These factors, combined with the polymer sensitivity to aging, explain the relatively lower than the expected values while remaining consistent with literature reports for neat PIM-1 [14,79,93–96].

Additionally, as shown in Tables S2 and S3, the obtained average aging rate values over 60 days for CO_2 permeability (Barrer/day) are approximately in the range of (−5.6 to −2.4) for the mixed gas permeability and in the range of (−6.5 to −3.3) for single gas permeability, indicating that they are consistent with those observed for other PIMs as reported in previous publications [95,98]. Furthermore, the results indicate that the aging rate for pristine PIM-1 is faster and higher than for PIM-1/MXene MMMs in both single and mixed gas measurements. This lower aging rate in PIM-1/MXene MMMs can be attributed to several factors. The MXene particles provide physical cross-linking within the polymer matrix, which restricts polymer chain mobility and reduces the rate of structural relaxation and densification. Also, the MXene's barrier properties may slow down the diffusion of small gas molecules, reducing the overall permeability loss over time. Furthermore, the presence of MXene can enhance the rigidity of the polymer network, making it less susceptible to the free volume collapse that typically occurs during aging in pristine PIM-1 [23–26].

In summary, the current research underscores the promising prospective of MXene/PIM-1 MMMs as highly effective membrane materials for both mixed and single CO_2/CH_4 separation performance avoiding aging to a certain extent. Moreover, the obtained results highlight the significance of attaining a uniform dispersion of the MXene nanosheets within MXene/PIM-1 MMMs for achieving optimal gas perm-selectivity.

Furthermore, as shown in Fig. 9, MMMs incorporating MXene nanosheets at loadings from 1 to 5 wt% exhibit highly beneficial separation performance, outperforming pristine PIM-1 and even slightly surpassing the upper-bound Robeson line established in 2008 [5,12,99]. Notably, the MXene/PIM-1 (5 wt%) MMMs achieved the most remarkable results in both CO_2 permeability of 7652 Barrer and CO_2/CH_4 mixed selectivity of 13.8 prior to physical aging. The highest loading of MXene filler was established at 5 wt% due to the instability in the mechanical properties, as shown in the Fig. S3, for the MXene/PIM-1 as an increasing in the filler loading up to 5 wt% has been found to induce

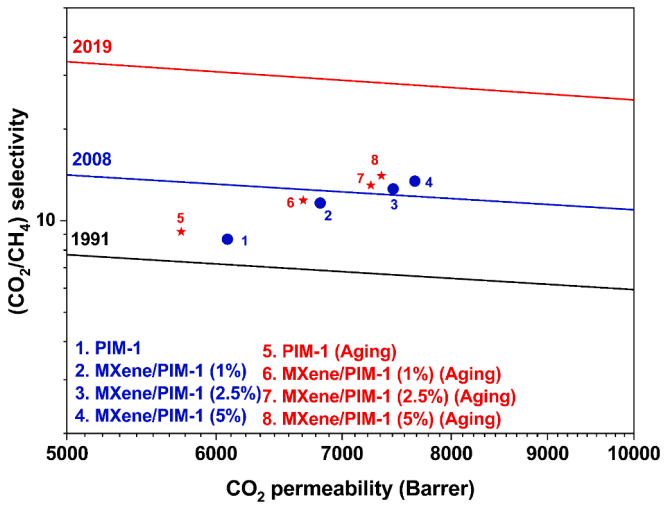

Fig. 9. CO_2/CH_4 mixed selectivity as a function of CO_2 permeability for PIM-1 and MXene/PIM-1 (1–5 wt%) MMMs, both before and after a 60-day aging period. 1991, 2008, and 2019 upper-bounds lines [4,12,99].

degradation within the MXene/PIM-1 MMMs, therefore no improvement in the separation performance.

Furthermore, the obtained results for MXene/PIM-1 MMMs were compared with MXene-based MMMs from literature [50,57,82–84]. Fig. S5 indicated that MXene/PIM-1 MMMs exhibit higher CO_2 permeability and lower CO_2/CH_4 selectivity for single gas measurements in compassion with the reported MXene based MMMs (Mainly Pebax-1675 [83], PEG-600 [57], Pebax-CMC [82], and cellulose triacetate (CTA) [84]). This might be attributed to PIM-1 having a highly interconnected network of micropores, which provides a large surface area for gas adsorption, therefore CO_2 molecules can easily penetrate these micropores due to their small size, leading to high gas uptake [20–22]. Additionally, PIM-1 possesses a high degree of free volume within its structure. This free volume allows for greater mobility of gas molecules, facilitating faster diffusion through the polymer matrix [20–22]. In contrast, the higher permeable polymeric membranes like PIM-1 are suffering from plasticization phenomena leads to increased membrane permeability by inducing swelling or relaxation of polymer chains, creating additional free volume for easier gas molecule diffusion. However, this process can also decrease selectivity by altering membrane morphology or enhancing the diffusion rates of both CO_2 and CH_4, reducing the membrane's ability to differentiate between them [25,85,87,100,101]. Additionally, the greater influx of CO_2 and CH_4 molecules into the membrane at higher permeabilities increases competition for sorption sites, further diminishing the membrane selectivity in favor of CO_2 over CH_4. Furthermore, as has been demonstrated throughout this manuscript, the presence of MXene as a filler given its sieving and adsorption capacity significantly improves permeability and selectivity. The findings align with the upper-bounds trade-off between permeability and selectivity in membrane materials. As permeability increases, selectivity tends to decrease, and vice versa [4,12,99], providing this time a high CO_2 permeability with not very penalized CO_2/CH_4 selectivity as the current values are over the 1991 line with the PIM-1 and over the 2008 line with the best MMM membrane.

Additionally, the solubility and diffusion coefficients obtained from time-lag experiments are presented in Fig. 10 and Table S4 (supplementary information). As illustrated, the MXene/PIM-1 MMMs exhibit significantly higher solubility and diffusion coefficients compared to the pristine PIM-1 membrane. This enhancement is attributed to the incorporation of MXene nanosheets, which increase the available free volume and create additional pathways for gas transport. The MXene nanosheets also introduce functional groups that interact

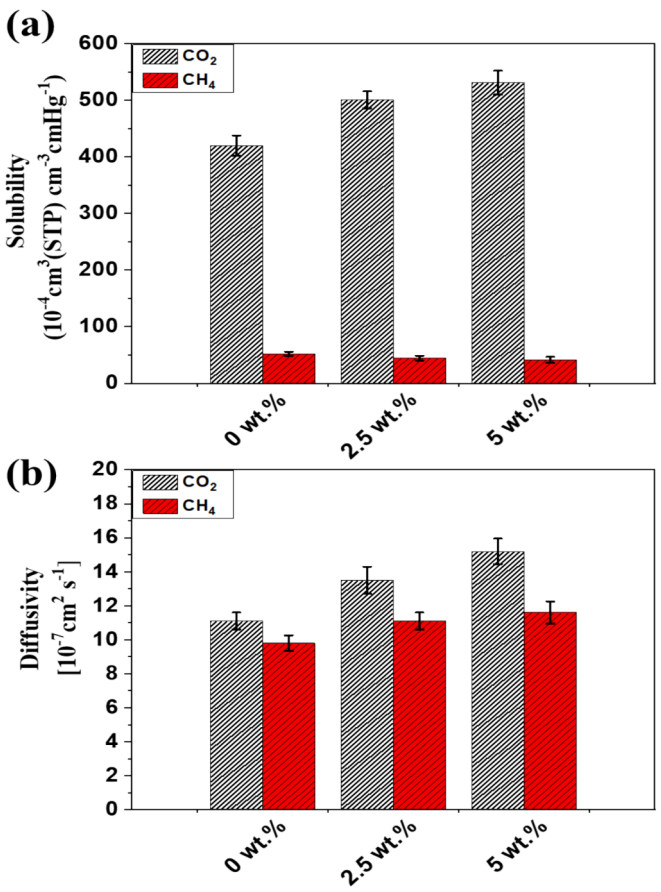

Fig. 10. (a) Solubility and (b) diffusivity coefficients measured by time lag for PIM-1 and MXene/PIM-1 (2.5 and 5 wt%) at 3 bar and 35 °C.

favorably with CO_2, improving gas sorption and diffusion. With the progressive increase in MXene loading (2.5 wt% and 5 wt%), there is a noticeable rise in both solubility (S) and diffusion (D) coefficients. This increment in S and D enhances the overall permeability and selectivity of the membranes, particularly for CO_2/CH_4 separation. The increase in solubility selectivity is more pronounced (see Table S4), reflecting the strong affinity of MXene for CO_2, while the slight rise in diffusion selectivity suggests that the molecular sieving effect is also moderately enhanced. Consequently, the MXene/PIM-1 (5 wt%) MMM demonstrates superior gas separation performance, with higher overall permeability and selectivity than the lower MXene-loaded membranes and the pure PIM-1 membrane. Additionally, the results obtained from solubility and diffusivity are in agreement with the previous reported data for PIM-1 membrane [93,102–106]. This demonstrates the effectiveness of MXene nanosheets in enhancing membrane performance for gas separation. The findings clearly show that incorporating higher amounts of MXene nanosheets significantly enhances the membrane's gas separation capabilities.

4. Conclusion

This study demonstrates the effective incorporation of MXene nanosheets into polymer PIM-1 to produce mixed matrix membranes (MMMs) with notable improvements in CO_2 permeability and CO_2/CH_4 selectivity compared to the pristine PIM-1 membrane. In agreement with the XRD and BET SSA measurements carried out, these enhancements can be attributed to the existence of the MXene particles and exacerbation of polar groups of MXene upon LiCl treatment, which enhance the filler-polymer interaction and the membrane affinity for preferential adsorption and diffusion of CO_2 over CH_4. As the MXene filler loading increased (in the 0–5 wt% range), the separation performance improved even more, surpassing the Robeson upper-bound line established in 2008. While aging led to a decrease in the CO_2 permeability, there was a notable increase in CO_2/CH_4 selectivity within all the fabricated MMMs. Despite these alterations, the MMMs consistently outperformed the pristine polymer membrane with a good permeability-selectivity balance. It should be noted that MXene, although its exfoliation was not very high, has been obtained with HCl acid treatment instead of the more hazardous HF, this treatment being sufficient to obtain good separation results.

Additionally, the incorporating of MXene filler within PIM-1 matrix resulted in an increase in CO_2/CH_4 selectivity with 1–5 wt% MXene filler loading and demonstrated superior separation performance when compared to pristine PIM-1, achieving a CO_2/CH_4 separation selectivity of 13.5 at 7652 Barrer of CO_2 permeability at 5 wt% filler loading. Despite a decline in the CO_2 permeability over time with aging (60 days), there was a slight increase in the CO_2/CH_4 selectivity (up to 4.3 % at 5 wt% MXene filler loading) and slight decrease in the CO_2 permeability across all MMMs, with the best results achieved for 5 wt% MXene/PIM-1 MMM (CO_2/CH_4 separation selectivity of 14.0 at 7345 Barrer of CO_2 permeability). The reduction in permeability caused by aging is less in the MMMs than in the pure PIM-1 membrane, so the introduction of MXene limits the movements of the polymer chains, mitigating physical aging. Additionally, the permeation tests were consistent when comparing both mixed and single gas results obtained under the same experimental conditions, as well as with the time lag ones.

Furthermore, the incorporating MXene nanosheets into MXene/PIM-1 MMMs significantly enhances gas separation performance by increasing solubility and diffusion coefficients, particularly for CO_2/CH_4 separation, as higher MXene content results in improved permeability and selectivity, demonstrating the effectiveness of MXene in enhancing the membrane separation performance.

Summarizing, this study provides valuable insights by investigating the influence of MXene filler loading and aging on the membrane performance, setting the stage for additional fine-tuning and exploration of MXene/PIM-1 MMMs as a sustainable technology for biogas upgrading and for extension to gas membrane separation.

CRediT authorship contribution statement

Mohamed Yahia: Investigation, Methodology, Validation, Formal analysis, Visualization, Writing – original draft, Writing – review & editing. **Dalia Refaat:** Investigation, Validation, Formal analysis. **Joaquín Coronas:** Conceptualization, Methodology, Visualization, Supervision, Funding acquisition, Writing – original draft, Writing – review & editing. **Carlos Tellez:** Conceptualization, Methodology, Visualization, Supervision, Funding acquisition, Writing – original draft, Writing – review & editing.

Declaration of competing interest

The authors declare that they have no known competing financial interests or personal relationships that could have appeared to influence the work reported in this paper.

Data availability

Data will be made available on request.

Acknowledgments

This recent investigation is acknowledging the grants: 1. PID2019-104009RB-I00 (funded by MICIU/AEI/10.13039/501100011033/), 2. PID2022-138582OB-I00 (funded by MICIU/AEI/10.13039/501100011033/ and by "ERDF A way of making Europe"), 3. TED2021-

130621B-C4 (funded by MICIU/AEI/10.13039/501100011033/ and The "European Union Next-Generation-EU/PRTR"), 4. CEX2023-001286-S funded by MICIU/AEI/10.13039/501100011033. M. Yahia's is supported through "the María Zambrano program" funded by both "the European Union's Next-Generation-EU" and "the Spanish Ministerio de Universidades". Financial assistance from "the Government of Aragón (T68_23R)" is also recognized. Furthermore, technical guidance and instrumentation provided by "the Universidad de Zaragoza/UNIZAR" through "the national facility ELECMI ICTS", "the Servicio General de Apoyo a la Investigación-SAI", and "Laboratorio de Microscopías Avanzadas", are appreciated.

Appendix A. Supplementary data

Supplementary data to this article can be found online at https://doi.org/10.1016/j.seppur.2024.129825.

References

[1] Y. Zhang, J. Sunarso, S. Liu, R. Wang, Current status and development of membranes for CO_2/CH_4 separation: A review, Int. J. Greenhouse Gas Control 12 (2013) 84–107.
[2] H. Yang, Z. Xu, M. Fan, R. Gupta, R.B. Slimane, A.E. Bland, I. Wright, Progress in carbon dioxide separation and capture: A review, J. Environ. Sci. 20 (1) (2008) 14–27.
[3] B.D. Freeman, Basis of permeability/selectivity tradeoff relations in polymeric gas separation membranes, Macromolecules 32 (2) (1999) 375–380.
[4] L.M. Robeson, Correlation of separation factor versus permeability for polymeric membranes, J. Membr. Sci. 62 (2) (1991) 165–185.
[5] L.M. Robeson, B.D. Freeman, D.R. Paul, B.W. Rowe, An empirical correlation of gas permeability and permselectivity in polymers and its theoretical basis, J. Membr. Sci. 341 (1–2) (2009) 178–185.
[6] S. Basu, A.L. Khan, A. Cano-Odena, C. Liu, I.F.J. Vankelecom, Membrane-based technologies for biogas separations, Chem. Soc. Rev. 39 (2) (2010) 750–768.
[7] X. Zou, G. Zhu, Microporous organic materials for membrane-based gas separation, Adv. Mater. 30 (3) (2018) 1700750.
[8] R.W. Baker, B.T. Low, Gas separation membrane materials: a perspective, Macromolecules 47 (20) (2014) 6999–7013.
[9] S. Wang, X. Li, H. Wu, Z. Tian, Q. Xin, G. He, D. Peng, S. Chen, Y. Yin, Z. Jiang, M. D. Guiver, Advances in high permeability polymer-based membrane materials for CO_2 separations, Energ. Environ. Sci. 9 (6) (2016) 1863–1890, https://doi.org/10.1039/C6EE00811A.
[10] G. Dong, H. Li, V. Chen, Challenges and opportunities for mixed-matrix membranes for gas separation, J. Mater. Chem. A 1 (15) (2013) 4610–4630.
[11] M.R. Khdhayyer, E. Esposito, A. Fuoco, M. Monteleone, L. Giorno, J.C. Jansen, M. P. Attfield, P.M. Budd, Mixed matrix membranes based on UiO-66 MOFs in the polymer of intrinsic microporosity PIM-1, Sep. Purif. Technol. 173 (2017) 304–313.
[12] L.M. Robeson, The upper bound revisited, J. Membr. Sci. 320 (1) (2008) 390–400, https://doi.org/10.1016/j.memsci.2008.04.030.
[13] C.E. Powell, G.G. Qiao, Polymeric CO_2/N_2 gas separation membranes for the capture of carbon dioxide from power plant flue gases, J. Membr. Sci. 279 (1–2) (2006) 1–49.
[14] M. Yahia, Q.N.P. Le, N. Ismail, M. Essalhi, O. Sundman, A. Rahimpour, M.M. Dal-Cin, N. Tavajohi, Effect of incorporating different ZIF-8 crystal sizes in the polymer of intrinsic microporosity, PIM-1, for CO_2/CH_4 separation, Microporous Mesoporous Mater. 312 (2021) 110761.
[15] T.-S. Chung, L.Y. Jiang, Y. Li, S. Kulprathipanja, Mixed matrix membranes (MMMs) comprising organic polymers with dispersed inorganic fillers for gas separation, Prog. Polym. Sci. 32 (4) (2007) 483–507.
[16] N.A.H.M. Nordin, A.F. Ismail, A. Mustafa, R.S. Murali, T. Matsuura, Utilizing low ZIF-8 loading for an asymmetric PSf/ZIF-8 mixed matrix membrane for CO_2/CH_4 separation, RSC Adv. 5 (38) (2015) 30206–30215.
[17] Y. Li, T.-S. Chung, C. Cao, S. Kulprathipanja, The effects of polymer chain rigidification, zeolite pore size and pore blockage on polyethersulfone (PES)-zeolite A mixed matrix membranes, J. Membr. Sci. 260 (1–2) (2005) 45–55.
[18] D.-Y. Kang, J.S. Lee, Challenges in Developing MOF-Based Membranes for Gas Separation, Langmuir 39 (8) (2023) 2871–2880.
[19] M. Pérez-Miana, J.M. Luque-Alled, M. Yahia, Á. Mayoral, J. Coronas, ZIF-8 modified with 2-undecylimidazolate as filler for mixed matrix membranes for CO_2 separation, J. Mater. Chem. A (2024), https://doi.org/10.1039/D3TA07109J.
[20] C.A. Scholes, S. Kanehashi, Polymer of intrinsic microporosity (PIM-1) membranes treated with supercritical CO_2, Membranes 9 (3) (2019) 41.
[21] N.B. McKeown, P.M. Budd, Polymers of intrinsic microporosity (PIMs): organic materials for membrane separations, heterogeneous catalysis and hydrogen storage, Chem. Soc. Rev. 35 (8) (2006) 675–683.
[22] N.B. McKeown, The structure-property relationships of Polymers of Intrinsic Microporosity (PIMs), Curr. Opin. Chem. Eng. 36 (2022) 100785, https://doi.org/10.1016/j.coche.2021.100785.
[23] M. Tamaddondar, A.B. Foster, M. Carta, P. Gorgojo, N.B. McKeown, P.M. Budd, Mitigation of Physical Aging with Mixed Matrix Membranes Based on Cross-Linked PIM-1 Fillers and PIM-1, ACS Appl. Mater. Interfaces 12 (41) (2020) 46756–46766, https://doi.org/10.1021/acsami.0c13838.
[24] S. He, B. Zhu, S. Li, Y. Zhang, X. Jiang, C.H. Lau, L. Shao, Recent progress in PIM-1 based membranes for sustainable CO_2 separations: Polymer structure manipulation and mixed matrix membrane design, Sep. Purif. Technol. 284 (2022) 120277.
[25] R.R. Tiwari, J. Jin, B.D. Freeman, D.R. Paul, Physical aging, CO_2 sorption and plasticization in thin films of polymer with intrinsic microporosity (PIM-1), J. Membr. Sci. 537 (2017) 362–371, https://doi.org/10.1016/j.memsci.2017.04.069.
[26] M.Z. Ahmad, R. Castro-Muñoz, P.M. Budd, Boosting gas separation performance and suppressing the physical aging of polymers of intrinsic microporosity (PIM-1) by nanomaterial blending, Nanoscale 12 (46) (2020) 23333–23370, https://doi.org/10.1039/D0NR07042D.
[27] B. Seoane, J. Coronas, I. Gascon, M.E. Benavides, O. Karvan, J. Caro, F. Kapteijn, J. Gascon, Metal–organic framework based mixed matrix membranes: a solution for highly efficient CO_2 capture? Chem. Soc. Rev. 44 (8) (2015) 2421–2454, https://doi.org/10.1039/C4CS00437J.
[28] X. Li, Y. Cheng, H. Zhang, S. Wang, Z. Jiang, R. Guo, H. Wu, Efficient CO_2 Capture by Functionalized Graphene Oxide Nanosheets as Fillers To Fabricate Multi-Permselective Mixed Matrix Membranes, ACS Appl. Mater. Interfaces 7 (9) (2015) 5528–5537, https://doi.org/10.1021/acsami.5b00106.
[29] B. Zornoza, B. Seoane, J.M. Zamaro, C. Téllez, J. Coronas, Combination of MOFs and Zeolites for Mixed-Matrix Membranes, ChemPhysChem 12 (15) (2011) 2781–2785, https://doi.org/10.1002/cphc.201100583.
[30] G. Dong, J. Hou, J. Wang, Y. Zhang, V. Chen, J. Liu, Enhanced CO_2/N_2 separation by porous reduced graphene oxide/Pebax mixed matrix membranes, J. Membr. Sci. 520 (2016) 860–868, https://doi.org/10.1016/j.memsci.2016.08.059.
[31] L. Chen, G. Shi, J. Shen, B. Peng, B. Zhang, Y. Wang, F. Bian, J. Wang, D. Li, Z. Qian, G. Xu, G. Liu, J. Zeng, L. Zhang, Y. Yang, G. Zhou, M. Wu, W. Jin, J. Li, H. Fang, Ion sieving in graphene oxide membranes via cationic control of interlayer spacing, Nature 550 (7676) (2017) 380–383, https://doi.org/10.1038/nature24044.
[32] J.M. Luque-Alled, C. Moreno, P. Gorgojo, Two-dimensional materials for gas separation membranes, Curr. Opin. Chem. Eng. 39 (2023) 100901, https://doi.org/10.1016/j.coche.2023.100901.
[33] J. Shen, G. Liu, Y. Ji, Q. Liu, L. Cheng, K. Guan, M. Zhang, G. Liu, J. Xiong, J. Yang, W. Jin, 2D MXene Nanofilms with Tunable Gas Transport Channels, Adv. Funct. Mater. 28 (31) (2018) 1801511, https://doi.org/10.1002/adfm.201801511.
[34] G. Liu, L. Cheng, G. Chen, F. Liang, G. Liu, W. Jin, Pebax-Based Membrane Filled with Two-Dimensional Mxene Nanosheets for Efficient CO_2 Capture, Chemistry – An Asian Journal 15(15) (2020) 2364-2370. https://doi.org/10.1002/asia.201901433.
[35] L. Ding, Y. Wei, L. Li, T. Zhang, H. Wang, J. Xue, L.-X. Ding, S. Wang, J. Caro, Y. Gogotsi, MXene molecular sieving membranes for highly efficient gas separation, Nat. Commun. 9 (1) (2018) 155, https://doi.org/10.1038/s41467-017-02529-6.
[36] L. Ding, Y. Wei, Y. Wang, H. Chen, J. Caro, H. Wang, A Two-Dimensional Lamellar Membrane: MXene Nanosheet Stacks, Angew. Chem. Int. Ed. 56 (7) (2017) 1825–1829, https://doi.org/10.1002/anie.201609306.
[37] B. Anasori, M.R. Lukatskaya, Y. Gogotsi, 2D metal carbides and nitrides (MXenes) for energy storage, Nat. Rev. Mater. 2 (2) (2017) 16098, https://doi.org/10.1038/natrevmats.2016.98.
[38] M. Naguib, M. Kurtoglu, V. Presser, J. Lu, J. Niu, M. Heon, L. Hultman, Y. Gogotsi, M.W. Barsoum, Two-Dimensional Nanocrystals Produced by Exfoliation of Ti_3AlC_2, Adv. Mater. 23 (37) (2011) 4248–4253, https://doi.org/10.1002/adma.201102306.
[39] M. Naguib, V.N. Mochalin, M.W. Barsoum, Y. Gogotsi, Two-Dimensional Materials: 25th Anniversary Article: MXenes: A New Family of Two-Dimensional Materials (Adv. Mater. 7/2014), Advanced Materials 26(7) (2014) 982-982. https://doi.org/10.1002/adma.201470041.
[40] Q. Shi, Y. Zhong, M. Wu, H. Wang, H. Wang, High-Performance Sodium Metal Anodes Enabled by a Bifunctional Potassium Salt, Angew. Chem. Int. Ed. 57 (29) (2018) 9069–9072, https://doi.org/10.1002/anie.201803049.
[41] K. Hantanasirisakul, M.-Q. Zhao, P. Urbankowski, J. Halim, B. Anasori, S. Kota, C. E. Ren, M.W. Barsoum, Y. Gogotsi, Fabrication of $Ti_3C_2T_x$ MXene Transparent Thin Films with Tunable Optoelectronic Properties, Adv. Electron. Mater. 2 (6) (2016) 1600050, https://doi.org/10.1002/aelm.201600050.
[42] G. Murali, J.K. Reddy Modigunta, Y.H. Park, J.-H. Lee, J. Rawal, S.-Y. Lee, I. In, S.-J. Park, A Review on MXene Synthesis, Stability, and Photocatalytic Applications, ACS Nano 16(9) (2022) 13370-13429. https://doi.org/10.1021/acsnano.2c04750.
[43] T. Liu, X. Liu, N. Graham, W. Yu, K. Sun, Two-dimensional MXene incorporated graphene oxide composite membrane with enhanced water purification performance, J. Membr. Sci. 593 (2020) 117431, https://doi.org/10.1016/j.memsci.2019.117431.
[44] B. Meng, G. Liu, Y. Mao, F. Liang, G. Liu, W. Jin, Fabrication of surface-charged MXene membrane and its application for water desalination, J. Membr. Sci. 623 (2021) 119076, https://doi.org/10.1016/j.memsci.2021.119076.
[45] K.M. Kang, D.W. Kim, C.E. Ren, K.M. Cho, S.J. Kim, J.H. Choi, Y.T. Nam, Y. Gogotsi, H.-T. Jung, Selective Molecular Separation on $Ti_3C_2T_x$–Graphene Oxide Membranes during Pressure-Driven Filtration: Comparison with Graphene

Oxide and MXenes, ACS Appl. Mater. Interfaces 9 (51) (2017) 44687–44694, https://doi.org/10.1021/acsami.7b10932.
[46] F. Shi, J. Sun, J. Wang, M. Liu, Z. Yan, B. Zhu, Y. Li, X. Cao, MXene versus graphene oxide: Investigation on the effects of 2D nanosheets in mixed matrix membranes for CO_2 separation, J. Membr. Sci. 620 (2021) 118850, https://doi.org/10.1016/j.memsci.2020.118850.
[47] A.P. Isfahani, A. Arabi Shamsabadi, M. Soroush, MXenes and Other Two-Dimensional Materials for Membrane Gas Separation: Progress, Challenges, and Potential of MXene-Based Membranes, Industrial & Engineering Chemistry Research 62(5) (2023) 2309-2328. https://doi.org/10.1021/acs.iecr.2c02042.
[48] S. Venkateshalu, A.N. Grace, MXenes—A new class of 2D layered materials: Synthesis, properties, applications as supercapacitor electrode and beyond, Appl. Mater. Today 18 (2020) 100509, https://doi.org/10.1016/j.apmt.2019.100509.
[49] Y. Fan, L. Wei, X. Meng, W. Zhang, N. Yang, Y. Jin, X. Wang, M. Zhao, S. Liu, An unprecedented high-temperature-tolerance 2D laminar MXene membrane for ultrafast hydrogen sieving, J. Membr. Sci. 569 (2019) 117–123, https://doi.org/10.1016/j.memsci.2018.10.017.
[50] M.M. Lichaei, J. Thibault, Mixed matrix membranes based on two-dimensional materials for efficient CO_2 separation: A comprehensive review, Process Saf. Environ. Prot. 183 (2024) 952–975, https://doi.org/10.1016/j.psep.2024.01.069.
[51] I. Ahmad, H. Jee, S.H. Song, M.J. Kim, T. Eisa, J.K. Jang, K.J. Chae, C.Y. Chuah, E. Yang, Delaminated or multilayer $Ti_3C_2T_X$-MXene-incorporated polydimethylsiloxane mixed-matrix membrane for enhancing CO_2/N_2 separation, Materials Today Sustainability 23 (2023) 100410, https://doi.org/10.1016/j.mtsust.2023.100410.
[52] Z. Hu, Y. Yang, X.-F. Zhang, C. Xu, J. Yao, Integrating two-dimensional MXene fillers into nanocellulose for the fabrication of CO_2 separation membranes, Sep. Purif. Technol. 326 (2023) 124704, https://doi.org/10.1016/j.seppur.2023.124704.
[53] C. Wang, J. Wu, Y. Wang, P. Cheng, S. Sun, T. Wang, Z. Lei, X. Niu, L. Xu, CO_2-Philic Nanocomposite Polymer Matrix Incorporated with MXene Nanosheets for Ultraefficient CO_2 Capture, ACS Appl. Mater. Interfaces 16 (11) (2024) 14152–14161, https://doi.org/10.1021/acsami.3c19504.
[54] K. Wang, D. Chen, J. Tang, Z. Hong, Z. Zhu, Z. Yuan, Z. Lin, Y. Liu, R. Semiat, X. He, PIM-1-based membranes mediated with CO_2-philic MXene nanosheets for superior CO_2/N_2 separation, Chem. Eng. J. 483 (2024) 149305, https://doi.org/10.1016/j.cej.2024.149305.
[55] M.D. Guiver, M. Yahia, M.M. Dal-Cin, G.P. Robertson, S. Saeedi Garakani, N. Du, N. Tavajohi, Gas Transport in a Polymer of Intrinsic Microporosity (PIM-1) Substituted with Pseudo-Ionic Liquid Tetrazole-Type Structures, Macromolecules 53(20) (2020) 8951-8959. https://doi.org/10.1021/acs.macromol.0c01321.
[56] M. Alhabeb, K. Maleski, B. Anasori, P. Lelyukh, L. Clark, S. Sin, Y. Gogotsi, Guidelines for Synthesis and Processing of Two-Dimensional Titanium Carbide ($Ti_3C_2T_x$ MXene), Chem. Mater. 29 (18) (2017) 7633–7644, https://doi.org/10.1021/acs.chemmater.7b02847.
[57] W. Luo, Z. Niu, P. Mu, J. Li, MXene/poly(ethylene glycol) mixed matrix membranes with excellent permeance for highly efficient separation of CO_2/N_2 and CO_2/CH_4, Colloids Surf A Physicochem Eng Asp 640 (2022) 128481, https://doi.org/10.1016/j.colsurfa.2022.128481.
[58] M.R. Hasan, H. Zhao, N. Steunou, C. Serre, M. Malankowska, C. Téllez, J. Coronas, Optimization of MIL-178(Fe) and Pebax® 3533 loading in mixed matrix membranes for CO_2 capture, Int. J. Greenhouse Gas Control 121 (2022) 103791, https://doi.org/10.1016/j.ijggc.2022.103791.
[59] A. Fuoco, M. Monteleone, E. Esposito, R. Bruno, J. Ferrando-Soria, E. Pardo, D. Armentano, J.C. Jansen, Gas Transport in Mixed Matrix Membranes: Two Methods for Time Lag Determination, Computation, 2020.
[60] S.S. Dhingra, E. Marand, Mixed gas transport study through polymeric membranes, J. Membr. Sci. 141 (1) (1998) 45–63, https://doi.org/10.1016/S0376-7388(97)00285-8.
[61] L. Martínez-Izquierdo, A. Perea-Cachero, M. Malankowska, C. Téllez, J. Coronas, A comparative study between single gas and mixed gas permeation of polyether-block-amide type copolymer membranes, J. Environ. Chem. Eng. 10 (5) (2022) 108324, https://doi.org/10.1016/j.jece.2022.108324.
[62] N.U. Kiran, A.B. Deore, M.A. More, D.J. Late, C.S. Rout, P. Mane, B. Chakraborty, L. Besra, S. Chatterjee, Comparative Study of Cold Electron Emission from 2D $Ti_3C_2T_x$ MXene Nanosheets with Respect to Its Precursor Ti_3SiC_2 MAX Phase, ACS Applied Electronic Materials 4 (6) (2022) 2656–2666, https://doi.org/10.1021/acsaelm.2c00128.
[63] H. Heydari, S. Salehian, S. Amiri, M. Soltanieh, S.A. Musavi, UV-cured polyvinyl alcohol-MXene mixed matrix membranes for enhancing pervaporation performance in dehydration of ethanol, Polym. Test. 123 (2023) 108046, https://doi.org/10.1016/j.polymertesting.2023.108046.
[64] Y. Zhao, L.V. Goncharova, Q. Zhang, P. Kaghazchi, Q. Sun, A. Lushington, B. Wang, R. Li, X. Sun, Inorganic-Organic Coating via Molecular Layer Deposition Enables Long Life Sodium Metal Anode, Nano Lett. 17 (9) (2017) 5653–5659, https://doi.org/10.1021/acs.nanolett.7b02464.
[65] L. Hao, K.-S. Liao, T.-S. Chung, Photo-oxidative PIM-1 based mixed matrix membranes with superior gas separation performance, J. Mater. Chem. A 3 (33) (2015) 17273–17281.
[66] P.M. Budd, B.S. Ghanem, S. Makhseed, N.B. McKeown, K.J. Msayib, C. E. Tattershall, Polymers of intrinsic microporosity (PIMs): robust, solution-processable, organic nanoporous materials, Chem. Commun. 2 (2004) 230–231, https://doi.org/10.1039/B311764B.
[67] N.B. McKeown, P.M. Budd, K.J. Msayib, B.S. Ghanem, H.J. Kingston, C. E. Tattershall, S. Makhseed, K.J. Reynolds, D. Fritsch, Polymers of Intrinsic Microporosity (PIMs): Bridging the Void between Microporous and Polymeric Materials, Chemistry – A, European Journal 11 (9) (2005) 2610–2620, https://doi.org/10.1002/chem.200400860.
[68] N.B. McKeown, Polymers of Intrinsic Microporosity (PIMs), Polymer 202 (2020) 122736, https://doi.org/10.1016/j.polymer.2020.122736.
[69] M. Tian, S. Rochat, H. Fawcett, A.D. Burrows, C.R. Bowen, T.J. Mays, Chemical modification of the polymer of intrinsic microporosity PIM-1 for enhanced hydrogen storage, Adsorption 26 (7) (2020) 1083–1091, https://doi.org/10.1007/s10450-020-00239-y.
[70] J. Jeromenok, J. Weber, Restricted Access: On the Nature of Adsorption/Desorption Hysteresis in Amorphous, Microporous Polymeric Materials, Langmuir 29 (42) (2013) 12982–12989, https://doi.org/10.1021/la402630s.
[71] P. Srimuk, F. Kaasik, B. Krüner, A. Tolosa, S. Fleischmann, N. Jäckel, M.C. Tekeli, M. Aslan, M.E. Suss, V. Presser, MXene as a novel intercalation-type pseudocapacitive cathode and anode for capacitive deionization, J. Mater. Chem. A 4 (47) (2016) 18265–18271, https://doi.org/10.1039/C6TA07833H.
[72] S. Ghotia, A. Kumar, V. Sudarsan, N. Dwivedi, S. Singh, P. Kumar, Multilayered $Ti_3C_2T_x$ MXenes: A prominent materials for hydrogen storage, Int. J. Hydrogen Energy 52 (2024) 100–107, https://doi.org/10.1016/j.ijhydene.2023.05.145.
[73] M.L. Jue, C.S. McKay, B.A. McCool, M.G. Finn, R.P. Lively, Effect of Nonsolvent Treatments on the Microstructure of PIM-1, Macromolecules 48 (16) (2015) 5780–5790, https://doi.org/10.1021/acs.macromol.5b01507.
[74] W. Han, C. Zhang, M. Zhao, F. Yang, Y. Yang, Y. Weng, Post-modification of PIM-1 and simultaneously in situ synthesis of porous polymer networks into PIM-1 matrix to enhance CO_2 separation performance, J. Membr. Sci. 636 (2021) 119544, https://doi.org/10.1016/j.memsci.2021.119544.
[75] F. Cacho-Bailo, C. Téllez, J. Coronas, Interactive Thermal Effects on Metal-Organic Framework Polymer Composite Membranes, Chemistry – A, European Journal 22 (28) (2016) 9533–9536, https://doi.org/10.1002/chem.201601530.
[76] S. Basu, A. Cano-Odena, I.F.J. Vankelecom, MOF-containing mixed-matrix membranes for CO_2/CH_4 and CO_2/N_2 binary gas mixture separations, Sep. Purif. Technol. 81 (1) (2011) 31–40, https://doi.org/10.1016/j.seppur.2011.06.037.
[77] Y. Liu, J. Zhang, X. Tan, High Performance of PIM-1/ZIF-8 Composite Membranes for O_2/N_2 Separation, ACS Omega 4 (15) (2019) 16572–16577, https://doi.org/10.1021/acsomega.9b02363.
[78] A. Ghorai, A. Midya, R. Maiti, S.K. Ray, Exfoliation of WS2 in the semiconducting phase using a group of lithium halides: a new method of Li intercalation, Dalton Trans. 45 (38) (2016) 14979–14987, https://doi.org/10.1039/C6DT02823C.
[79] M. Balçık, S.B. Tantekin-Ersolmaz, I. Pinnau, M.G. Ahunbay, CO_2/CH_4 mixed-gas separation in PIM-1 at high pressures: Bridging atomistic simulations with process modeling, J. Membr. Sci. 640 (2021) 119838.
[80] R. Khan, M.T. Mehran, S.R. Naqvi, A.H. Khoja, M.M. Baig, M.A. Akram, F. Shahzad, S. Hussain, A highly efficient A-site deficient perovskite interlaced within two dimensional MXene nanosheets as an active electrocatalyst for hydrogen production, Int. J. Hydrogen Energy 47 (88) (2022) 37476–37489, https://doi.org/10.1016/j.ijhydene.2021.09.017.
[81] R.B. Rakhi, B. Ahmed, D. Anjum, H.N. Alshareef, Direct Chemical Synthesis of MnO2 Nanowhiskers on Transition-Metal Carbide Surfaces for Supercapacitor Applications, ACS Appl. Mater. Interfaces 8 (29) (2016) 18806–18814, https://doi.org/10.1021/acsami.6b04481.
[82] W. Luo, Z. Niu, P. Mu, J. Li, Pebax and CMC@MXene-Based Mixed Matrix Membrane with High Mechanical Strength for the Highly Efficient Capture of CO_2, Macromolecules 55 (21) (2022) 9851–9859, https://doi.org/10.1021/acs.macromol.2c01532.
[83] W. Guan, X. Yang, C. Dong, X. Yan, W. Zheng, Y. Xi, X. Ruan, Y. Dai, G. He, Prestructured MXene fillers with uniform channels to enhance CO_2 selective permeation in mixed matrix membranes, J. Appl. Polym. Sci. 138 (8) (2021) 49895, https://doi.org/10.1002/app.49895.
[84] C. Regmi, S. Ashtiani, F. Průša, K. Friess, Synergistic effect of hybridized TNT@GO fillers in CTA-based mixed matrix membranes for selective CO_2/CH_4 separation, Sep. Purif. Technol. 282 (2022) 120128, https://doi.org/10.1016/j.seppur.2021.120128.
[85] P. Bernardo, F. Bazzarelli, F. Tasselli, G. Clarizia, C.R. Mason, L. Maynard-Atem, P.M. Budd, M. Lanč, K. Pilnáček, O. Vopička, K. Friess, D. Fritsch, Y. P. Yampolskii, V. Shantarovich, J.C. Jansen, Effect of physical aging on the gas transport and sorption in PIM-1 membranes, Polymer 113 (2017) 283–294, https://doi.org/10.1016/j.polymer.2016.10.040.
[86] S. Harms, K. Rätzke, F. Faupel, N. Chaukura, P.M. Budd, W. Egger, L. Ravelli, Aging and Free Volume in a Polymer of Intrinsic Microporosity (PIM-1), J. Adhes. 88 (7) (2012) 608–619, https://doi.org/10.1080/00218464.2012.682902.
[87] R. Swaidan, B. Ghanem, E. Litwiller, I. Pinnau, Physical Aging, Plasticization and Their Effects on Gas Permeation in “Rigid” Polymers of Intrinsic Microporosity, Macromolecules 48 (18) (2015) 6553–6561, https://doi.org/10.1021/acs.macromol.5b01581.
[88] R. Swaidan, B. Ghanem, M. Al-Saeedi, E. Litwiller, I. Pinnau, Role of Intrachain Rigidity in the Plasticization of Intrinsically Microporous Triptycene-Based Polyimide Membranes in Mixed-Gas CO_2/CH_4 Separations, Macromolecules 47 (21) (2014) 7453–7462, https://doi.org/10.1021/ma501798v.
[89] C. Geng, Y. Sun, Z. Zhang, Z. Qiao, C. Zhong, Mitigated Aging in a Defective Metal-Organic Framework Pillared Polymer of an Intrinsic Porosity Hybrid Membrane for Efficient Gas Separation, ACS Sustain. Chem. Eng. 10 (11) (2022) 3643–3650.
[90] K. Chen, L. Ni, H. Zhang, C. Xiao, L. Li, X. Guo, J. Qi, C. Wang, X. Sun, J. Li, Incorporating KAUST-7 into PIM-1 towards mixed matrix membranes with long-term stable CO_2/CH_4 separation performance, J. Membr. Sci. 661 (2022) 120848.

[91] E. Aliyev, J. Warfsmann, B. Tokay, S. Shishatskiy, Y.-J. Lee, J. Lillepaerg, N. R. Champness, V. Filiz, Gas transport properties of the metal–organic framework (MOF)-assisted polymer of intrinsic microporosity (PIM-1) thin-film composite membranes, ACS Sustain. Chem. Eng. 9 (2) (2020) 684–694.
[92] S. Thomas, I. Pinnau, N. Du, M.D. Guiver, Pure- and mixed-gas permeation properties of a microporous spirobisindane-based ladder polymer (PIM-1), J. Membr. Sci. 333 (1) (2009) 125–131, https://doi.org/10.1016/j.memsci.2009.02.003.
[93] A.E. Gemeda, M.G. De Angelis, N. Du, N. Li, M.D. Guiver, G.C. Sarti, Mixed gas sorption in glassy polymeric membranes. III. CO_2/CH_4 mixtures in a polymer of intrinsic microporosity (PIM-1): Effect of temperature, Journal of Membrane Science 524 (2017) 746-757. https://doi.org/10.1016/j.memsci.2016.11.053.
[94] R. Swaidan, B.S. Ghanem, E. Litwiller, I. Pinnau, Pure- and mixed-gas CO_2/CH_4 separation properties of PIM-1 and an amidoxime-functionalized PIM-1, J. Membr. Sci. 457 (2014) 95–102, https://doi.org/10.1016/j.memsci.2014.01.055.
[95] M. Yahia, L.A. Lozano, J.M. Zamaro, C. Téllez, J. Coronas, Microwave-assisted synthesis of metal–organic frameworks UiO-66 and MOF-808 for enhanced CO_2/CH_4 separation in PIM-1 mixed matrix membranes, Sep. Purif. Technol. 330 (2024) 125558, https://doi.org/10.1016/j.seppur.2023.125558.
[96] J. Ahn, W.-J. Chung, I. Pinnau, J. Song, N. Du, G.P. Robertson, M.D. Guiver, Gas transport behavior of mixed-matrix membranes composed of silica nanoparticles in a polymer of intrinsic microporosity (PIM-1), J. Membr. Sci. 346 (2) (2010) 280–287, https://doi.org/10.1016/j.memsci.2009.09.047.
[97] A.F. Bushell, M.P. Attfield, C.R. Mason, P.M. Budd, Y. Yampolskii, L. Starannikova, A. Rebrov, F. Bazzarelli, P. Bernardo, J. Carolus Jansen, M. Lanč, K. Friess, V. Shantarovich, V. Gustov, V. Isaeva, Gas permeation parameters of mixed matrix membranes based on the polymer of intrinsic microporosity PIM-1 and the zeolitic imidazolate framework ZIF-8, Journal of Membrane Science 427 (2013) 48-62. https://doi.org/10.1016/j.memsci.2012.09.035.
[98] Z. Xu, Z.L. Croft, D. Guo, K. Cao, G. Liu, Recent development of polyimides: Synthesis, processing, and application in gas separation, J. Polym. Sci. 59 (11) (2021) 943–962, https://doi.org/10.1002/pol.20210001.
[99] B. Comesaña-Gándara, J. Chen, C.G. Bezzu, M. Carta, I. Rose, M.-C. Ferrari, E. Esposito, A. Fuoco, J.C. Jansen, N.B. McKeown, Redefining the Robeson upper bounds for CO_2/CH_4 and CO_2/N_2 separations using a series of ultrapermeable benzotriptycene-based polymers of intrinsic microporosity, Energ. Environ. Sci. 12 (9) (2019) 2733–2740, https://doi.org/10.1039/C9EE01384A.
[100] M.S. Suleman, K.K. Lau, Y.F. Yeong, Plasticization and Swelling in Polymeric Membranes in CO_2 Removal from Natural Gas, Chem. Eng. Technol. 39 (9) (2016) 1604–1616, https://doi.org/10.1002/ceat.201500495.
[101] T. Visser, N. Masetto, M. Wessling, Materials dependence of mixed gas plasticization behavior in asymmetric membranes, J. Membr. Sci. 306 (1) (2007) 16–28, https://doi.org/10.1016/j.memsci.2007.07.048.
[102] T.H. Lee, T. Joo, P. Jean-Baptiste, P.A. Dean, J.Y. Yeo, Z.P. Smith, Fine-tuning ultramicroporosity in PIM-1 membranes by aldehyde functionalization for efficient hydrogen separation, J. Mater. Chem. A (2024), https://doi.org/10.1039/D4TA04082A.
[103] P. Li, T.S. Chung, D.R. Paul, Gas sorption and permeation in PIM-1, J. Membr. Sci. 432 (2013) 50–57, https://doi.org/10.1016/j.memsci.2013.01.009.
[104] P.M. Budd, K.J. Msayib, C.E. Tattershall, B.S. Ghanem, K.J. Reynolds, N. B. McKeown, D. Fritsch, Gas separation membranes from polymers of intrinsic microporosity, J. Membr. Sci. 251 (1) (2005) 263–269, https://doi.org/10.1016/j.memsci.2005.01.009.
[105] W. Ji, K. Li, Y.-G. Min, W. Shi, J. Li, X. Ma, Remarkably enhanced gas separation properties of PIM-1 at sub-ambient temperatures, J. Membr. Sci. 623 (2021) 119091, https://doi.org/10.1016/j.memsci.2021.119091.
[106] G. Genduso, Y. Wang, B.S. Ghanem, I. Pinnau, Permeation, sorption, and diffusion of CO_2-CH_4 mixtures in polymers of intrinsic microporosity: The effect of intrachain rigidity on plasticization resistance, J. Membr. Sci. 584 (2019) 100–109, https://doi.org/10.1016/j.memsci.2019.05.014.